# Influence of non-local strain regularization on the evolution of shear bands

B. Schädlich & H.F. Schweiger
*Institute for Soil Mechanics and Foundation Engineering, Graz University of Technology, Austria*

ABSTRACT

The numerical analysis of strain softening problems by means of the conventional finite element method is well known to suffer from severe mesh dependency, and various approaches have been proposed to overcome this deficiency. Among these, the non-local approach has received increasing attention over the last two decades due to its relatively simple implementation and mechanically plausible assumptions. In this study the consequences of different assumptions for the non-local strain regularization are investigated with regard to the evolution of shear bands. A partially non-local approach has been implemented into a multilaminate constitutive model. The constitutive model employs a Hvorslev surface to describe peak shear strength and dilatancy in the heavily overconsolidated range. It is shown that the numerical shear band in biaxial test simulations rotates in softening and settles at ~45° if softening is allowed to spread to stress points outside the initial shear band. This contradicts experimental findings, which show much steeper and virtually constant shear bands. Limiting strain regularization to stress points at or close to failure provides significantly better match with the experimental data.

Keywords: Non-local approach, Hvorslev surface, multilaminate model, strain softening

## 1 INTRODUCTION

Strain softening, i.e. reduction of shear strength with accumulating deformations, is a commonly observed phenomenon in geomaterials like rocks, dense sands and stiff, overconsolidated clays. Due to loosening of the material and destruction of the initial soil fabric, the load bearing capacity of the soil reduces after the maximum shear strength is mobilized, and approaches a critical state at sufficiently large deformations. Post-peak deformations concentrate in narrow shear bands, whose size is governed by the average grain size of the material.

While these effects are well known from experimental investigations, numerical simulation of strain softening e.g. with the finite element method is hampered by severe mesh dependency. The size of the finite elements provides an internal length scale, which governs the rate of post-peak strain softening and the size of the numerical shear band. Consequently, the numerical softening behavior is heavily influenced by the coarseness of the finite element mesh.

In this study non-local strain regularization is employed to obtain mesh independent results. This approach is based on averaging the plastic strains in the vicinity of the current stress point.

The non-local approach is implemented into a multilaminate constitutive model which can account for the shear strength and dilatancy of heavily overconsolidated clays.

The major objective of this paper is to show the impact of different assumptions for the non-local approach on the evolution of shear bands. Two versions of the non-local approach are compared: The first version employs strain regularization only in the post-peak region, and strain averaging is confined to stress points which are already in softening. In the second version, regularization is carried out also before peak strength is mobilized, and softening can spread to stress points which have not fully mobilized their peak shear strength yet. Numerical results of biaxial test simulations employing both models are compared with experimental results and analytical solutions.

## 2 MULTILAMINATE HVORSLEV SURFACE MODEL

The multilaminate constitutive model employed in this study is described in detail in [1]. Therefore only the features relevant for this study are reported here.

### *2.1 Multilaminate framework*

Multilaminate constitutive models are based on the idea that the material behavior can be formulated on a distinct number of so-called integration planes with varying orientation. Each plane *i* represents a sector of a virtual sphere of unit radius around the stress point and is assigned a weight factor $w_i$ according to the proportion of its sector with regard to the volume of the unit sphere. The global plastic strain increment $d\boldsymbol{\varepsilon}_{gl}^{pl}$ to a prescribed load increment is obtained by summation of the contributions of all planes.

$$\boldsymbol{\sigma}_{i,loc} = \left(\sigma_{n,i} \quad \tau_{s,i} \quad \tau_{t,i}\right)^T = \left(\mathbf{T}_i\right)^T \cdot \boldsymbol{\sigma}_{gl} \tag{1}$$

$$\mathbf{T}_i = \frac{\partial \boldsymbol{\sigma}_{i,loc}}{\partial \boldsymbol{\sigma}_{gl}} \tag{2}$$

$$d\boldsymbol{\varepsilon}_{gl}^{pl} = 3 \cdot \sum_i \mathbf{T}_i \cdot d\boldsymbol{\varepsilon}_{i,loc}^{pl} \cdot w_i \tag{3}$$

$$d\boldsymbol{\varepsilon}_{i,loc}^{pl} = \left(\varepsilon_{n,pl} \quad \gamma_{s,pl} \quad \gamma_{t,pl}\right)^T \tag{4}$$

### *2.2 Yield and plastic potentials functions*

Local plastic strain increments $d\boldsymbol{\varepsilon}_{gl}^{pl}$ are calculated according to plasticity theory on integration plane level. Yield and plastic potential functions are formulated in local shear and normal stresses, $\tau = (\tau_s^2 + \tau_t^2)^{0.5}$ and $\sigma'_n$, and local plastic shear and normal strains, $\gamma_{pl} = (\gamma_{s,pl}^2 + \gamma_{t,pl}^2)^{0.5}$ and $\varepsilon_{n,pl}$, respectively. Yield surfaces are mobilized separately on all integration planes in anisotropic loading, thus accounting for anisotropy induced by plastic strains.

Three yield surfaces are defined in the model (Figure 1). The elliptical, fully associated cap yield surface $f_{cap}$ controls the behavior in compression and is defined by the pre-consolidation pressure $\sigma'_{nc}$. In deviatoric loading the shear yield surface $f_{cone}$ gets activated, which is controlled by the mobilized friction angle $\phi'_m$. Non-associated plasticity is employed for the cone yield surface, with the direction of the plastic strain increment given by the angle of dilatancy, $\psi$. Mobilization of dilatancy is defined by a cubical function in dependency on $\phi'_m$ [2].

The Hvorslev yield surface $f_{HV}$ is connected to $f_{cap}$ at the critical state line and can be considered as the shear strength envelope on integration plane level.

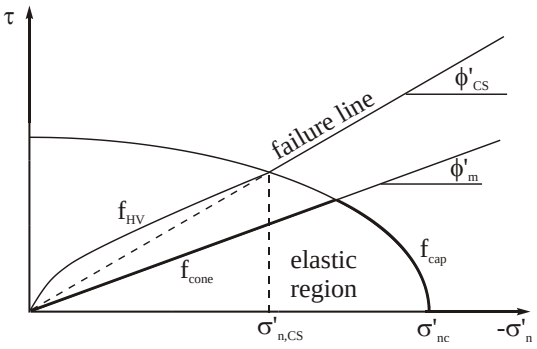


Figure 1: Local yield surfaces

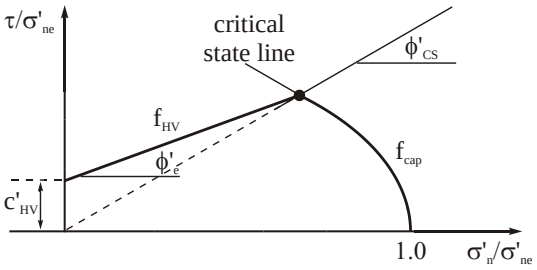


Figure 2: Local normalized shear strength envelope

$$f_{HV} = \tau + \sigma'_n \cdot \tan\varphi'_e - c'_{HV} \tag{5}$$

$$c'_{HV} = B \cdot \left( \frac{\tan\varphi'_e}{\tan\varphi'_{CS}} - 1 \right) \cdot \sigma'_{ne} \tag{6}$$

The Hvorslev surface plots as a straight line in a normalized $\tau/\sigma'_{ne}$ vs. $\sigma'_n/\sigma'_{ne}$ diagram (with $\sigma'_{ne}$ being the equivalent pressure on the local normal compression line), defined by the angle $\phi'_e$ (Figure 2). The position of the Hvorslev surface changes with the size of the cap yield surface and vice versa. Positive plastic normal strains, caused by dilatancy at the Hvorslev yield surface, reduce $\sigma'_{nc}$, whereas negative (compressive) plastic normal strains from the cap yield surface enlarge $\sigma'_{nc}$. Hardening rules of the cap and cone yield surface are described in detail in [1].

In the heavily overconsolidated range (left of the critical state line in Figure 2), dilatancy is governed by the distance of the current stress state to the critical state line (Figure 3).

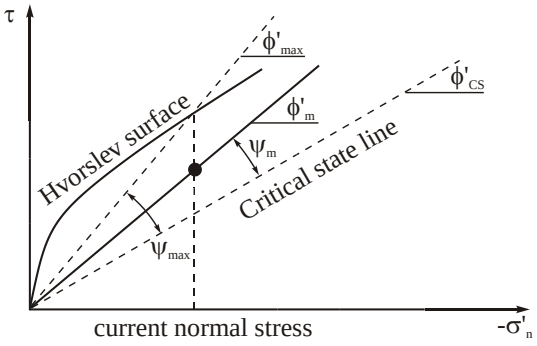


Figure 3: Mobilized and maximum angle of dilatancy

The maximum angle of dilatancy, $\psi_{max}$, is obtained from the difference between Hvorslev surface and the critical state friction angle $\phi'_{CS}$. As the Hvorslev surface reduces in size after the peak shear strength is mobilized, strain softening is initiated and the soil approaches the critical state with $\psi_m = \psi_{max} = 0$.

### *2.3 Strain softening*

Strain softening is induced by the evolution of dilatant plastic strains, which result in contraction of the cap and Hvorslev yield surface. The plastic strains of the cone and Hvorslev surface are summed up and multiplied with the softening parameter $h_{soft}$ to obtain the damage strain $\varepsilon_{di}$ (equation 9). In a first version of the model (labeled 'reference' further on), reduction of $\sigma'_{nc}$ in softening is only calculated from the damage strain accumulated after peak strength has been mobilized (equation 8). Therefore, only plastic strains from the Hvorslev yield surface contribute to strain softening. In the 'modified' version of the model, $\sigma'_{nc}$ is already reduced before the initial peak strength is reached due to dilatancy at the cone yield surface above the critical state line (equation 7). Consequently, failure in the modified model occurs slightly below the peak strength of the reference model (Figure 4).

Reference:

$$\sigma'_{nc,soft} = -\left[ \left|\sigma'_{nc}\right|^{1-m} + K \cdot \frac{(m-1)}{p_{ref}^{m-1}} \cdot \left( \varepsilon^*_{di} - \varepsilon^*_{di,peak} \right) \right]^{\frac{1}{1-m}} \tag{7}$$

Modified:

$$\sigma'_{nc,soft} = -\left[ \left|\sigma'_{nc}\right|^{1-m} + K \cdot \frac{(m-1)}{p_{ref}^{m-1}} \cdot \varepsilon^*_{di} \right]^{\frac{1}{1-m}} \tag{8}$$

$$\varepsilon_{di} = h_{soft} \cdot \left( \varepsilon^p_{n,cone} + \varepsilon^p_{n,HV} \right) \tag{9}$$

Averaged, non-local quantities are marked by '*' and obtained as explained in the next section. $K$ is the volumetric hardening parameter, $m$ and $p_{ref}$ are the exponent and the reference stress of the stress dependent stiffness [1].

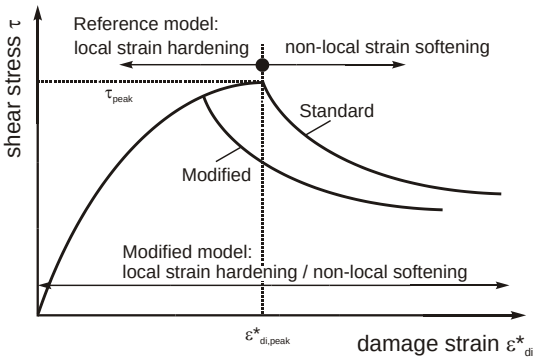


Figure 4: Schematic stress-strain curves of reference and modified strain softening model

## 3 NON-LOCAL STRAIN REGULARIZATION

A partially non-local approach has been employed in this study, in which only the damage strain $\varepsilon_d$ is treated as a non-local quantity. Local plastic strains $\varepsilon_{d,k}$ in the neighboring stress points $k$ are averaged to obtain the non-local damage strain $\varepsilon_d^*$ of the current stress point.

$$\varepsilon_d^* = \frac{1}{V_w} \cdot \sum_{k=1}^{k_{SP}} \varepsilon_{d,k} \cdot \omega'_k \cdot V_k \tag{10}$$

$$V_w = \sum_{k=1}^{k_{SP}} \omega'_k \cdot V_k \tag{11}$$

$$\omega'(r) = \frac{r}{l_{cal}^2} e^{-\left(\frac{r}{l_{cal}}\right)^2} \tag{12}$$

$k_{SP}$ is the number of stress points in the averaging area, $V_k$ is the soil volume assigned to stress point $k$, and $\omega'_k$ is the value of the weight function $\omega'$ at the stress point $k$. The weighting function $\omega'$ proposed by Galavi [2] is utilized (equation 12), which assigns zero weight to the current stress point. The internal length $l_{cal}$ determines the averaging area, and $r$ is the distance of stress point $k$ to the current stress point.

## 4 BIAXIAL TEST SIMULATIONS

### *4.1 Numerical model and material parameters*

Evolution of shear bands is studied in biaxial test simulations. The test specimen is 1.0 m high and 0.5 m wide, with very stiff and fully rough end-plates at the top and the bottom of the specimen. Drained plane strain conditions are applied. After applying initial stresses of $\sigma'_v = \sigma'_h = -100$ kPa, vertical displacement of the top end plate is gradually increased. A slight geometric shift of the top plate of 1 mm to the right has been applied to enforce the formation of a single shear band. Four different meshes with 84, 158, 334 and 646 15-noded triangular finite elements are used (Figure 5).

Material parameters are derived from undrained triaxial tests on reconstituted, overconsolidated Pietrafitta clay [3]. Derivation of the model parameters and the comparison of model predictions and experimental results is shown in [1]. Parameters relevant for the current study are listed in Table 1.

Table 1. Material parameters of Pietrafitta clay

| parameter | value |
|---|---|
| $E_{oed,ref}$ | 1020 kPa |
| $E_{ur,ref}$ | 8140 kPa |
| $p_{ref}$ | 100 kPa |
| $m$ | 1.0 |
| $\varphi'_{cs}$ | 30.0° |
| $\varphi'_e$ | 23.8° |
| $\sigma'_{nc}$ (initial) | -2000 kPa |
| $h_{soft}$ | 40 |
| $l_{cal}$ | 5 cm |

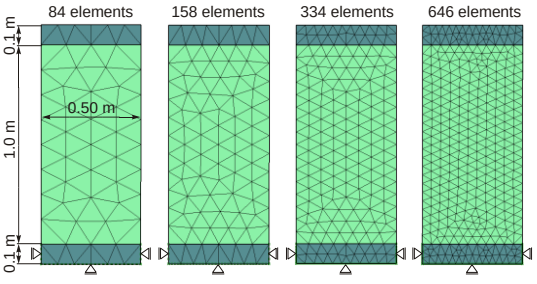


Figure 5: Numerical biaxial model and FE-meshes

### 4.2 *Reference model*

Load-displacement curves obtained with the reference model for the different FE meshes show sufficient regularization (Figure 6). Shear bands develop shortly after peak, starting from the shear strain concentration at the edges of the end plates, and maintain the same inclination throughout the simulation (Figure 7). Frictional strength and dilatancy predicted by the Hvorslev surface model can be back calculated from the stress ratio at failure as $\varphi'_{max}$ = 45.3° and $\psi_{max}$ = 15.3°. The inclination of the numerical shear bands to the horizontal is ~63° for all the FE meshes. This value is close to the Coulomb solution ($\Theta_C \approx 68°$, equation 13), which is governed by frictional strength. The Roscoe solution [4] (equation 14), which is based on kinematic considerations, delivers $\Theta_R \approx 53°$, which is significantly below the value obtained in the numerical simulations.

$$\theta_C = 45° + \varphi'_{\max} / 2 \tag{13}$$

$$\theta_R = 45° + \psi_{\max} / 2 \tag{14}$$

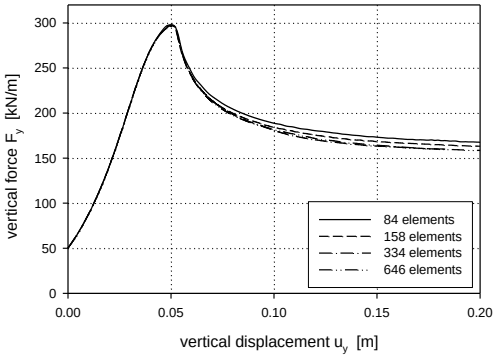


Figure 6: Load displacement curves with reference model

### 4.3 *Modified model*

Applying the modified model with non-local strain regularization in the pre-peak range also delivers virtually mesh-independent load-displacement curves. Shear band inclinations at residual load level, however, differ notably from the results of the reference model (Figure 8) for all FE meshes. While the shear band also starts to develop from the strain concentrations at the end plates at peak, the shear band starts to rotate in subsequent loading and approaches $\Theta \approx 45°$ at residual load level. That value coincides with the Roscoe solution for $\psi$ = 0. Varying the shear strength parameters of the material ($\varphi'_{CS}$, $\varphi'_e$) had no notable influence on the final shear band inclinations. Only when a very small internal length $l_{cal}$ was adopted (and the softening parameter $h_{soft}$ scaled down accordingly), the numerical shear band maintained its position in softening (Figure 9). A much finer FE-mesh had to be used in this case to ensure sufficient regularization.

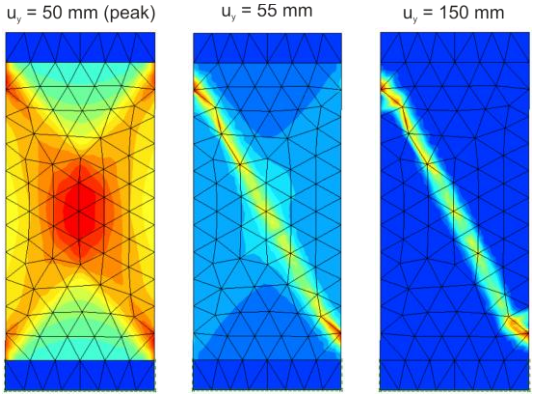


Figure 7: Shear band evolution with reference model (158 elements)

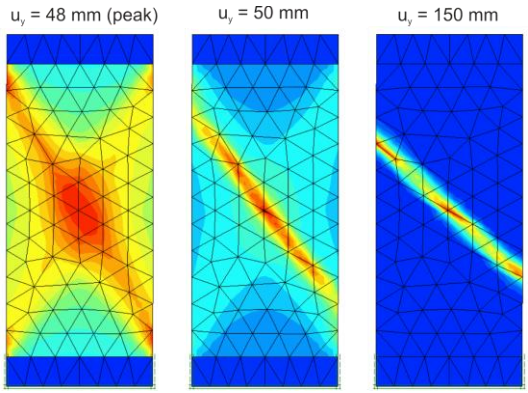


Figure 8: Shear band evolution with modified model (158 elements)

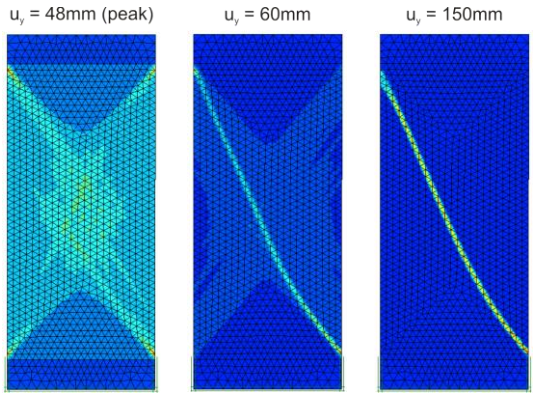


Figure 9: Shear band evolution with modified model for $l_{cal}$ = 1 cm, $h_{soft}$ = 3 (2440 elements)

## 5 CONCLUSIONS

The assumptions made in non-local strain regularization may strongly influence the evolution of shear bands obtained from the numerical model. If regularization is carried out only at the stress points which are already at failure (reference model), the shear band maintains its initial position and does not rotate notably with further loading. If regularization is extended to stress points which have not yet mobilized peak strength (modified model), softening is induced in the material adjacent to the shear band. Consequently, the shear band can easily change its position within the sample. In this case, shear bands settle at $\Theta \approx 45°$ at residual load level, which equals the Roscoe solution for $\psi = 0$ (critical state).

The tendency of FE simulations to predict the Roscoe solution in biaxial test simulations has been noted previously by other authors [5], and may be related to the rather large thickness of the numerical shear band compared to the outer dimensions of the numerical model. As shown analytically by Vermeer [6], kinematic boundary conditions become more influential with increasing thickness of the shear band, and hence shear bands will evolve along lines of zero extension, as predicted by the Roscoe solution. For very thin shear bands, static boundary conditions govern the orientation of the shear band, as predicted by the Coulomb solution. Experimental results support these considerations. The real shear band thickness is known to increase with the average grain size. Accordingly, fine sands and clays yield shear band orientations close to the Coulomb solution, while coarse grained gravel tends to yield the Roscoe solution [7]. In any case, however, rotation of shear bands – as obtained with the modified model - is not observed experimentally. Reducing shear strength in stress points outside the initial shear band therefore seems to be not appropriate to model the strain softening behavior of geomaterials.

Despite the distinct differences in the simulation of biaxial tests, the impact of these assumptions in the simulation of practical geotechnical problems remains to be investigated. In many practical cases, the geometry of the shear band is governed by geometrical constrains (external loads and structures), rather than by material properties. In this case it can be expected that both versions of the model will predict a very similar behavior.

## ACKNOWLEDGEMENT

The financial support for the first author by FWF Austria (grant no. P21225-N13) is gratefully acknowledged.

## REFERENCES

[1] Schädlich, B. 2012. A multilaminate constitutive model for stiff soils, Ph.D. thesis, Graz University of Technology.

[2] Schweiger, H.F., Wiltafsky, C., Scharinger, F. & Galavi, V. 2009. A multilaminate framework for modelling induced and inherent anisotropy of soils. *Géotechnique* **59** (2), 87-101.

[3] Burland, J.B., Rampello, S., Georgiannou, V.N. & Calabresi, G. 1996. A laboratory study of the strength of four stiff clays. *Géotechnique* **46** (3), 491-514.

[4] Roscoe, K. H. 1970. The influence of strains in soil mechanics. *Géotechnique* **20** (2), 129-170.

[5] Brinkgreve, R.B.J. 1994. Geomaterial models and numerical analysis of softening. Ph.D. thesis, Delft university press.

[6] Vermeer, P.A. 1990. The orientation of shear bands in biaxial tests. *Géotechnique* **40** (2), 223-236.

[7] Arthur, J.R.F. & Dunstan, T. 1982. Rupture layers in granular materials. Proc. IUTAM Conference on Deformation and Failure of Granular Materials, Vermeer & Luger (eds.), Delft. Netherlands, 453-459.